Attosecond strong-field interferometry in graphene: Chirality, singularity, and Berry phase

Hamed Koochaki Kelardeh,* Vadym Apalkov,† and Mark I. Stockman‡
Center for Nano-Optics (CeNO) and Department of Physics and Astronomy, Georgia State University, Atlanta, Georgia 30303, USA
(Received 11 February 2016; published 26 April 2016)

We propose an interferometry in graphene's reciprocal space without a magnetic field, employing strong ultrafast circularly polarized optical pulses. The reciprocal space interferograms contain information on the electronic spectra and topological properties of graphene and on the waveform and circular polarization of the excitation optical pulses. These can be measured using angle-resolved photoemission spectroscopy (ARPES) with attosecond ultraviolet pulses. The predicted effects provide unique opportunities in fundamental studies of two-dimensional topological materials and in applications to future petahertz light-wave-driven electronics.

DOI: 10.1103/PhysRevB.93.155434

I. INTRODUCTION

Graphene is a two-dimensional material with remarkable electronic properties: it is a gapless semiconductor (or, semimetal) where the valence band (VB) and conduction band (CB) touch each other at the Dirac points (K and K' points) in the reciprocal space where electrons and holes behave as massless fermions [1–3]. Electron band structure in graphene's reciprocal space is determined by its spatial and time-reversal symmetry. It is chiral, topologically nontrivial, and characterized by a nonzero Berry phase of $\pm\pi$ [1–6] acquired by the electronic wave function when circling around a K or K' point—see Fig. 1(a). This topologically nontrivial chiral structure of graphene manifest itself in the quantum Hall effect [1–3] and in angle-resolved photoemission spectroscopy (ARPES) [7]. The Berry phase has been observed in an optical-lattice quantum simulation of graphene in the presence of a magnetic field gradient (using the Stern-Gerlach effect) [6]. Similar measurements in natural graphene would require magnetic fields too high to be realistic. Note that the area of the present study is ultrafast electron kinetics in unbiased graphene and not graphene plasmons [8] that are absent in this case.

In this paper, we propose attosecond strong-field interferometry in graphene, which, without involvement of magnetic fields, reveals its chiral nature related to the Berry phase, and fundamentally allows measurement of the dynamic phase. It contains rich information about electronic structure, attosecond excitation dynamics, and, potentially, ultrafast relaxation in graphene. The idea of such strong-field interferometry is presented in Figs. 1(b)–1(f).

The quantum motion of an electron in the reciprocal space is known to be deterministic as expressed by the Bloch acceleration theorem, $\hbar\mathbf{k}(t) = \hbar\mathbf{k}_0 + e\mathbf{A}(t)$, where the vector potential is defined as $\mathbf{A}(t) = -\int_{-\infty}^{t}\mathbf{F}(t')dt'$, $\mathbf{k}(t)$ is the electron crystal momentum at time t, $\mathbf{k}_0$ is the crystal momentum at the initial time, e is unit charge, and $\mathbf{F}(t)$ is the optical electric field on graphene. We used optical pulses with a given number of oscillations defined in terms of Hermite polynomials [see Sec. II]. Each oscillation is circularly polarized. For an one-optical-oscillation ultrashort circularly polarized pulse, an example of the vector potential is displayed in Fig. 1(b) by the dashed red line. Assuming vacuum wavelength of 1500 nm, the optical period is $T = 5$ fs.

We consider laser pulses shorter than the electron scattering time ∼10–100 fs [13–18]. Hence the electron dynamics is coherent and can be described by time-dependent Schrödinger equation (see Sec. II). We solve numerically the time-dependent Schrödinger equation in the basis of the Houston functions [19]. Time-dependent expansion coefficients, $\beta_{v\mathbf{k}_0}(t)$ and $\beta_{c\mathbf{k}_0}(t)$, of the electron wave function in this basis determine the amplitudes for an electron with initial wave vector $\mathbf{k}_0$ to be in VB and CB, respectively. In graphene, the dipole matrix element $\mathbf{D}(\mathbf{k})$ between the VB and CB is singularly enhanced in the vicinity of the Dirac points [20], where most of transitions VB ↔ CB occur.

The set of the initial points for electron trajectories $\mathbf{k}(t)$, which pass through the K point, is a curve mirror-symmetric to the trajectory, as shown by the dark blue lines in Figs. 1(b)–1(d). This curve is a separatrix: electron trajectories that originate inside the separatrix encircle the K-point and thus accumulate the Berry phase [Fig. 1(c)], while those outside do not [Fig. 1(d)]. Due to the dipole singularity mentioned above in the previous paragraph, after an optical period, when the electron crystal momentum returns back to $\mathbf{k}_0$, the electrons excited to the VB will be situated in the vicinity of the separatrix. In the real-space Aharonov-Bohm effect [21], the incident electrons diffract and propagate to the observation point by two pathways around the magnetic flux region. In our case, there is no diffraction in the reciprocal space: the final electron momentum $\mathbf{k}$ is the same as the original one, $\mathbf{k}_0$. Thus a single-oscillation pulse does not create any interference fringes in the reciprocal space—cf. Fig. 2(a) to be discussed in detail later.

To have the desired interference of electrons, consider a pulse causing two passages in the K-point vicinity as schematically shown in Figs. 1(e) and 1(f). This pulse contains two periods with opposite circular polarizations, counter-rotating with respect to each other—an example of the optical fields is shown in the inset in Fig. 3. Ultrashort pulses containing opposite circular polarizations were synthesized for applications to generalized double optical gating (GDOG) [22].

In the case of counter-rotating polarizations, there are two pathways leading to the final momentum $\mathbf{k}_0$: (i) As shown

*hkoochakikelardeh1@student.gsu.edu
†vapalkov@gsu.edu
‡mstockman@gsu.edu

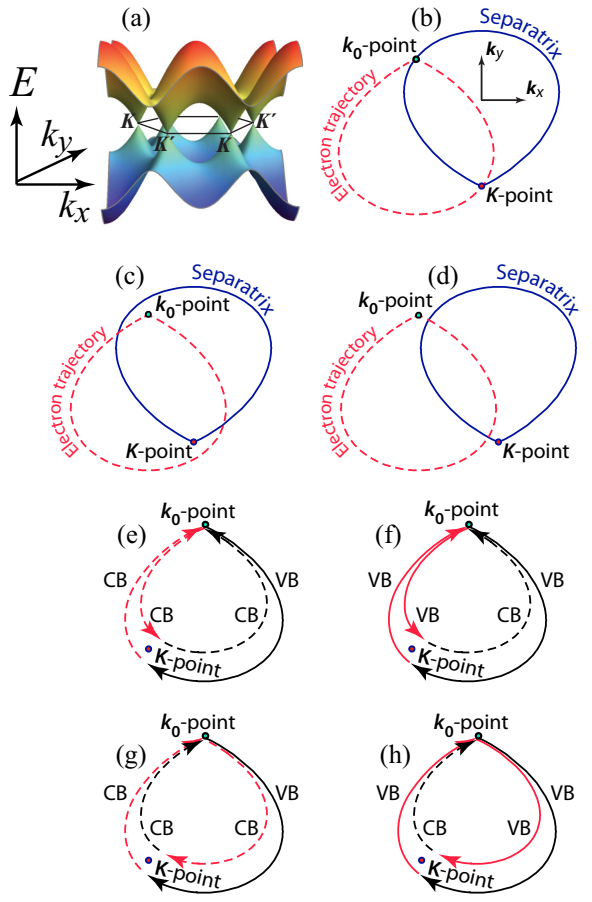

FIG. 1. Schematics of graphene electronic spectrum, reciprocal space trajectories, and separatrices. (a) Electron spectrum of graphene in the first Brillouin zone in tight binding model [9–12]. The six Dirac points are indicated as K and K', and the directions of coordinate axes are shown. (b)–(d) For a circularly polarized single-oscillation pulse, the separatrix is shown by solid blue lines and the electron trajectories starting at k_0 points are depicted by dashed red lines. For (b), (c), and (d), respectively, the k_0 point is on, inside, and outside of the separatrix. (e) and (f) Graphene as a self-referenced interferometer. The optical pulse contains two periods with opposite circularity: the first period, with some amplitude F_0, has the field rotating clockwise, and the second period with amplitude $0.75F_0$ has the field rotating counterclockwise. The electron motion in the VB is denoted by solid lines and in the CB by dashed lines. The red color highlights the segments of the trajectories where the electron motion for (e) and (f) occurs in different bands. (g) and (h) differ from (e) and (f) by the opposite circularity of the second period.

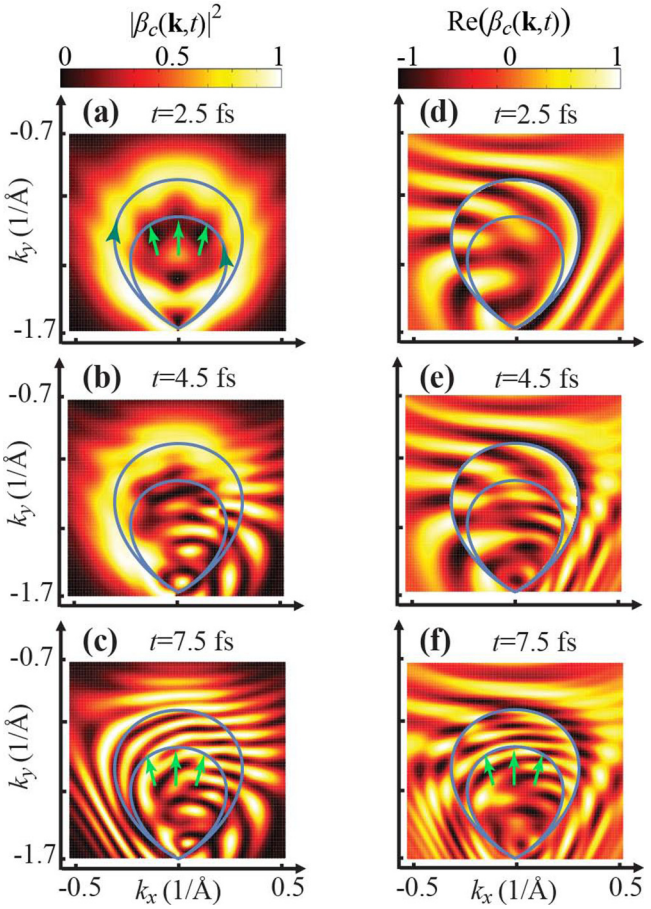

FIG. 2. Graphene interferograms in reciprocal space for the vicinity of the K point for different moments of time t. (a)–(c) For the instances of time t indicated, distributions of the CB population, $|\beta_c(\mathbf{k},t)|^2$, and (d)–(f) real part of the CB excitation amplitude, $\mathrm{Re}\beta_c(\mathbf{k},t)$. (a) The population distribution at the end of the first optical oscillations, $t = 2.5$ fs (the pulse start is set at $t = -2.5$ fs). The separatrices for the two oscillations are shown by blue lines and the directions of the optical electric field rotations are indicated by arrows. (b) The same as in (a) but for time $t = 4.5$ fs, i.e., in the initial stage of the second (counterclockwise) oscillation. (c) The same as in panel (b) but after the second oscillation is completed. (d)–(f) The same as (a)–(c) but for the CB excitation amplitude. The green arrows indicated the region where the bifurcations of the interference fringes occur.

in Fig. 1(e), an electron starts at $\mathbf{k}_0$, moves to the K-point, where it undergoes a transition VB $\rightarrow$ CB, and then returns to $\mathbf{k}_0$ and travels the second cycle entirely within the CB; (ii) Illustrated by Fig. 1(f), the electron dwells in the VB during the entire first cycle and undergoes the VB $\rightarrow$ CB transition in the vicinity of the K-point during the second cycle returning eventually to the $\mathbf{k}_0$ point. These two pathways are indistinguishable and their corresponding amplitudes, A_1 and A_2, interfere: the resulting population probability contains an interference term, $2\mathrm{Re}(A_1A_2^*) = 2|A_1A_2|\cos(\varphi_1 - \varphi_2)$. Note that the phase difference $\varphi_1 - \varphi_2$ between the two amplitudes, A_1 and A_2, accumulates only along the portions of their reciprocal space trajectories denoted by red in Figs. 1(e)-(f). This interferometer does not need an external reference source and, therefore, is self-referenced.

II. MODEL AND MAIN EQUATIONS

Consider ultrashort optical pulse with circular polarization. We start with a pulse consisting of two optical oscillation periods. These two periods may differ by the field amplitudes and directions of circular polarizations. We consider two cases: (i) the two optical periods have the same (say, left) circular polarization and (ii) the two optical periods have opposite (say, left and right) circular polarizations.

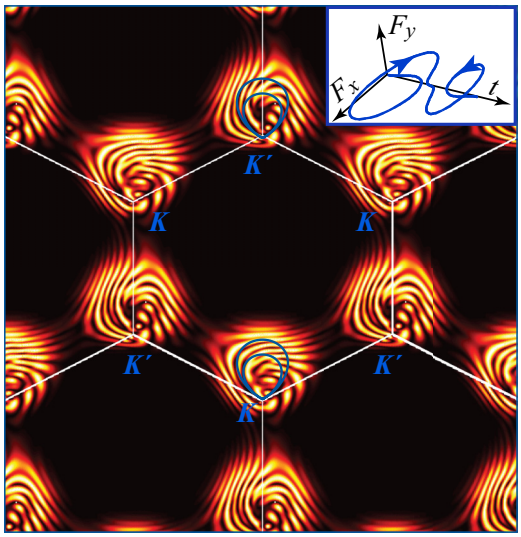

FIG. 3. Residual CB population in graphene after a two-oscillations pulse where the first optical cycle is left circularly-polarized with amplitude $F_0 = 0.5$ V/Å, and the second cycle is right circularly-polarized with amplitude $0.75F_0$ (this wave form is shown in the inset). The separatrices are indicated by blue lines superimposed on the distributions.

Consider for certainty a graphene monolayer positioned in the xy plane with the excitation light wave incident in the z direction. The pulse field is defined by its field vector (considered to be uniform inside graphene), $\mathbf{F} = \{F_x, F_y, 0\}$, which is parametrized in the form (derived from Hermite polynomials of the first and second order) as

$$F_x(t) = F_0[-e^{-u^2}(1-2u^2) \mp \alpha e^{-(u-u_0)^2}(1-2(u-u_0)^2)], \tag{1}$$

$$F_y(t) = 2F_0\left[ue^{-u^2} + \alpha(u-u_0)e^{-(u-u_0)^2}\right]. \tag{2}$$

Here, $\mp$ determines the circularities (the upper sign is for identical and the lower for opposite circular polarizations); F_0 is the amplitude of the first optical period, and αF_0 is the amplitude of the second optical period; $u = t/\tau$, $u_0 = t_0/\tau$, where τ is approximately quarter optical oscillation period, and t_0 is approximately a half pulse length. In specific computations, we set $\tau = 1$ fs and $t_0 = 5$ fs.

The Hamiltonian of an electron in graphene in the field of the optical pulse has the form

$$\mathcal{H} = \mathcal{H}_0 + e\mathbf{F}(t)\mathbf{r}, \tag{3}$$

where $\mathcal{H}_0$ is the field-free electron Hamiltonian, and $\mathbf{r} = (x, y)$ is a 2D radius vector in the plane of graphene. To describe the conduction and valence bands of graphene, we employ $\mathcal{H}_0$ in the nearest-neighbor tight-binding model [9–12]. In the reciprocal space, the Hamiltonian, $\mathcal{H}_0$, is a 2×2 matrix of the form [9,10]

$$\mathcal{H}_0 = \begin{pmatrix} 0 & \gamma f(\mathbf{k}) \\ \gamma f^*(\mathbf{k}) & 0 \end{pmatrix}, \tag{4}$$

where $\gamma = -3.03$ eV is the hopping integral and

$$f(\mathbf{k}) = \exp\left(i\frac{ak_x}{\sqrt{3}}\right) + 2\exp\left(-i\frac{ak_x}{2\sqrt{3}}\right)\cos\left(\frac{ak_y}{2}\right). \tag{5}$$

The energy spectrum of Hamiltonian $\mathcal{H}_0$ consists of the CB (π^* or antibonding band) and the VB (π or bonding band) with energy dispersion $E_c(\mathbf{k}) = -\gamma|f(\mathbf{k})|$ (CB) and $E_v(\mathbf{k}) = \gamma|f(\mathbf{k})|$ (VB). The corresponding wave functions for the VB (v) and the CB (c) are

$$\Psi_{\mathbf{k}}^{(c)}(\mathbf{r}) = \frac{e^{i\mathbf{kr}}}{\sqrt{2}}\begin{pmatrix} 1 \\ e^{-i\phi_k} \end{pmatrix} \tag{6}$$

and

$$\Psi_{\mathbf{k}}^{(v)}(\mathbf{r}) = \frac{e^{i\mathbf{kr}}}{\sqrt{2}}\begin{pmatrix} -1 \\ e^{-i\phi_k} \end{pmatrix}, \tag{7}$$

where $f(\mathbf{k}) = |f(\mathbf{k})|e^{i\phi_k}$. The wave functions $\Psi_{\mathbf{k}}^{(c)}$ and $\Psi_{\mathbf{k}}^{(v)}$ have two components belonging to sublattices A and B, respectively.

When the duration of the laser pulse is less than the characteristic electron scattering time, which is on the order of ~10–100 fs [13–18], the electron dynamics in external electric field of the optical pulse is coherent and can be described by the time dependent Schrödinger equation

$$i\hbar\frac{d\Psi}{dt} = \mathcal{H}\Psi, \tag{8}$$

where the Hamiltonian (3) has explicit time dependence.

The electric field of the optical pulse generates both interband and intraband electron dynamics. The interband dynamics introduces a coupling of the states of the CB and VB and results in redistribution of electrons between the two bands.

It is convenient to describe the intraband dynamics in the reciprocal space where it is described by the Bloch acceleration theorem [23],

$$\hbar\frac{d\mathbf{k}}{dt} = e\mathbf{F}(t). \tag{9}$$

This acceleration theorem is universal and does not depend on the dispersion law. Therefore the intraband electron dynamics is the same for both the VB and CB. For an electron with initial momentum $\mathbf{q}$, the temporal dynamics is described by the time-dependent wave vector, $\mathbf{k}_T(\mathbf{q},t)$, which is given by the solution of Eq. (9),

$$\mathbf{k}_T(\mathbf{q},t) = \mathbf{q} + \frac{e}{\hbar}\int_{-\infty}^{t}\mathbf{F}(t_1)dt_1. \tag{10}$$

The corresponding wave functions in the real space are the Houston functions, [19] $\Phi_{\alpha\mathbf{q}}^{(H)}(\mathbf{r},t)$,

$$\Phi_{\alpha\mathbf{q}}^{(H)}(\mathbf{r},t) = \Psi_{\mathbf{k}_T(\mathbf{q},t)}^{(\alpha)}(\mathbf{r})e^{-\frac{i}{\hbar}\int_{-\infty}^{t}dt_1 E_\alpha[\mathbf{k}_T(\mathbf{q},t_1)]}, \tag{11}$$

where $\alpha = v$ (for VB) or $\alpha = c$ (for CB).

Using the Houston functions as the basis, we express the general solution of the time-dependent Schrödinger equation (8) in the following form:

$$\Psi_{\mathbf{q}}(\mathbf{r},t) = \sum_{\alpha=v,c}\beta_{\alpha\mathbf{q}}(t)\Phi_{\alpha\mathbf{q}}^{(H)}(\mathbf{r},t). \tag{12}$$

The solution (12) is labeled by initial electron wave vector (crystal momentum) $\mathbf{q}$. Due to the universal electron dynamics in the reciprocal space, the states that belong to different bands (VB and CB) but have the same initial crystal momentum $\mathbf{q}$, will have the same crystal momentum $\mathbf{k}_T(\mathbf{q},t)$ at all moments of time t. Since the interband dipole matrix element, which determines the coupling of the VB and CB states in an external electric field, is diagonal in the reciprocal space, the states with different crystal momenta $\mathbf{q}$ are not coupled by the pulse field. As a result in Eq. (12), for each value of initial wave vector $\mathbf{q}$, we need to find only two time-dependent expansion coefficients $\beta_{v\mathbf{q}}(t)$ and $\beta_{c\mathbf{q}}(t)$. Such decoupling of the states with different values of $\mathbf{q}$ is a property of coherent dynamics. For incoherent dynamics, electron scattering couples states with different $\mathbf{q}$, and the dynamics may be described by density matrix formalism.

The expansion coefficients satisfy the following system of differential equations:

$$\frac{d\beta_{c\mathbf{q}}(t)}{dt} = -i\frac{\mathbf{F}(t)\mathbf{Q}_{\mathbf{q}}(t)}{\hbar}\beta_{v\mathbf{q}}(t), \tag{13}$$

$$\frac{d\beta_{v\mathbf{q}}(t)}{dt} = -i\frac{\mathbf{F}(t)\mathbf{Q}^{*}_{\mathbf{q}}(t)}{\hbar}\beta_{c\mathbf{q}}(t), \tag{14}$$

where the vector function $\mathbf{Q}_{\mathbf{q}}(t)$ is proportional to the interband dipole matrix element

$$\mathbf{Q}_{\mathbf{q}}(t) = \mathbf{D}[\mathbf{k}_T(\mathbf{q},t)]e^{-\frac{i}{\hbar}\int_{-\infty}^{t}dt_1\{E_c[\mathbf{k}_T(\mathbf{q},t_1)]-E_v[\mathbf{k}_T(\mathbf{q},t_1)]\}}, \tag{15}$$

where $\mathbf{D}(\mathbf{k}) = \{D_x(\mathbf{k}), D_y(\mathbf{k})\}$ is the dipole matrix element between the states of the VB and CB with wave vector $\mathbf{k}$, i.e.,

$$\mathbf{D}(\mathbf{k}) = \left\langle \Psi^{(c)}_{\mathbf{k}} \middle| e\mathbf{r} \middle| \Psi^{(v)}_{\mathbf{k}} \right\rangle. \tag{16}$$

Substituting the VB and CB wave functions (6) and (7) into Eq. (16), we obtain the following expressions for the interband dipole matrix elements

$$D_x(\mathbf{k}) = \frac{ea}{2\sqrt{3}}\frac{1+\cos\left(\frac{ak_y}{2}\right)\left[\cos\left(\frac{3ak_x}{2\sqrt{3}}\right)-2\cos\left(\frac{ak_y}{2}\right)\right]}{1+4\cos\left(\frac{ak_y}{2}\right)\left[\cos\left(\frac{3ak_x}{2\sqrt{3}}\right)+\cos\left(\frac{ak_y}{2}\right)\right]} \tag{17}$$

and

$$D_y(\mathbf{k}) = \frac{ea}{2}\frac{\sin\left(\frac{ak_y}{2}\right)\sin\left(\frac{3ak_x}{2\sqrt{3}}\right)}{1+4\cos\left(\frac{ak_y}{2}\right)\left[\cos\left(\frac{3ak_x}{2\sqrt{3}}\right)+\cos\left(\frac{ak_y}{2}\right)\right]}. \tag{18}$$

The system of Eqs. (13) and (14) describes the interband electron dynamics determining mixing of the VB and CB states in the electric field of the pulse. There are two solutions of the system (13) and (14), which correspond to two initial conditions: $(\beta_{v\mathbf{q}},\beta_{c\mathbf{q}}) = (1,0)$ and $(\beta_{v\mathbf{q}},\beta_{c\mathbf{q}}) = (0,1)$. These solutions determine the evolution of the states, which are initially in the VB and CB, respectively.

For undoped graphene, all states of the VB are occupied and all states of the CB are empty. For an electron, which is initially in the VB, the mixing of the states of different bands is characterized by the time-dependent excitation probability, $|\beta_{c\mathbf{q}}(t)|^2$. We can also define the time-dependent total occupation of the conduction band by the following expression:

$$\mathcal{N}_{CB}(t) = \sum_{\mathbf{q}} |\beta_{c\mathbf{q}}(t)|^2, \tag{19}$$

where the sum is over the first Brillouin zone.

III. RESULTS AND DISCUSSION

We use theory and parameters described above in Sec. II. We solve the Schrödinger numerically in the representation of the Houston functions. The results obtained are presented and discussed below in this section.

This process of the electron interferogram formation in the first Brillouin zone for a pulse containing two optical periods with opposite circularities is illustrated in Fig. 2. After the first full cycle (for $t = 2.5$ fs), the CB electron distribution density, $|\beta_c(\mathbf{k},t)|^2$, is shown in panel (a), and the real part of the CB population amplitude, $\mathrm{Re}\beta_c(\mathbf{k},t)$, is displayed in panel (d). The first optical oscillation does populate the CB along the corresponding separatrix but does not produce any interference fringes [panel (a)], while the population amplitude does show both the fringes and the Berry phase discontinuity by π [panel (d)].

During the second optical cycle, whose field amplitude, αF_0, is 75% of the first cycle amplitude, F_0 ($\alpha = 0.75$), there is gradual formation of the interference fringes in the direction of the electric field rotation along the second (smaller) separatrix [Fig. 2(b)], which is fully completed at the pulse end at $t = 7.5$ fs [Fig. 2(c)]. The interference fringes have characteristic bifurcations in the vicinity of the second separatrix as marked by the green arrows. The interferogram in panel (f) shows that at the positions of these bifurcations the dynamic phase changes very rapidly. Note that the Berry phases accumulated in the first and second quantum pathways to the final state [shown in Figs. 1(e) and 1(f)] are equal and, therefore, cancel out and do not show themselves as any discontinuities in the population interferograms [panel (c)]. These population interferograms [panels (a)–(c)] can, in principle, be directly observed by femtosecond ARPES.

The resulting reciprocal-space interferogram (the distribution of the CB population) in the extended Brillouin zone picture is displayed in Fig. 3. This distribution is highly chiral: there is pronounced right-left asymmetry determined by the chirality of the optical pulse (changing the circularity to the opposite would cause the distribution to be mirror-reflected in the yz plane—see Fig. 4 and its discussion). The interferograms at both the K and K' points are different, which reflects the intrinsic graphene chirality related to the Berry phase of graphene's reciprocal space.

The origin of this chirality can be understood from Figs. 1(e) and 1(f). When the second (counter-clockwise) oscillation begins at the initial point $\mathbf{k}_0$, which is close to the K point and is situated to the right of it, as shown in panel (e), the interfering portions of the trajectories (shown by the red) are short. The corresponding fringes are seen in Fig. 2(b) in the lower right part of the interferogram. In this case, time between the first and second passage of the K point is minimal, so any dephasing is small. Hence the phase increases fastest along the separatrix, which means that the fringes are normal to the separatrix, as

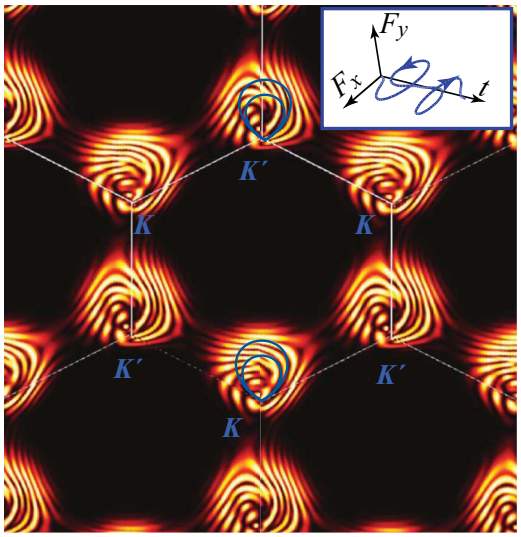

FIG. 4. Same as Fig. 3 but with for a pulse with opposite chirality. The first oscillation has its electric field rotating counter-clockwise, and the second oscillation does clockwise.

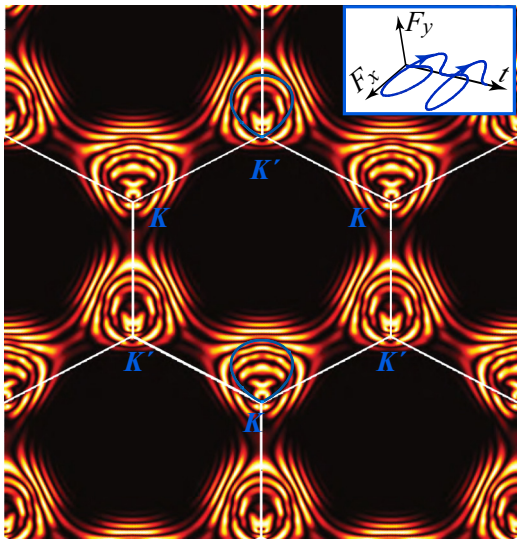

FIG. 5. The same as in Fig. 3 but for an optical pulse where the two optical periods have the same amplitudes and circular polarizations.

seen in Figs. 2(c) and 3. For the $\mathbf{k}_0$ points farther along the separatrix from the K-point, the time between the first and second passage of the K point increases up to the optical period, T. For such short pulses, the spectral width is large, $\Delta\omega \sim T^{-1}$. This large spectral width translates into a very fast collisionless dephasing (Landau damping [24]) whose time is $\sim\Delta\omega^{-1} \sim T$. Thus, at the left part of the interferogram, corresponding to longer times, there is little phase-difference along the separatrices, and the fringes tend to be parallel to the separatrices. To verify that the bifurcations originate from the second oscillation being of smaller amplitude, we have performed calculations for a pulse, which contains two periods with equal amplitudes; the same high degree of chirality is present but the bifurcations are absent (results not shown).

Figure 4 below demonstrates properties of exact spatial symmetry of graphene, namely, its symmetry with respect to reflection in the yz plane. This reflection leaves the system invariant but changes the sense of rotation of the field. As a result the interferogram in Fig. 4 is mirror-reflected in the yz axis with respect to that in Fig. 3.

In a sharp contrast to Figs. 3 and 4, a similar pulse consisting of two subpulses with identical circularity does not cause any interferogram chirality—see Fig. 5. The reason is that in this case the interfering segments of trajectories, shown in Figs. 1(g) and 1(h) by red lines, are extended over the entire optical period. This leads to two consequences. First, the time between the two interfering passages through the K point, in this case, is exactly the period T, there is strong dephasing, which causes the fringes to be mostly parallel to the separatrix—cf. Fig. 5. Second, because the field amplitudes for the two oscillations are equal, the amplitudes for the two pathways are complex-conjugated, $A_1 = A_2^*$, causing the distributions to be achiral (symmetric with respect to the reflection in the yz plane). However, the local distributions for the K and K' points are still different, which is due to the internal chirality of graphene's reciprocal space (Berry phase $\pm\pi$).

Though pulses with two optical oscillations are well within the state-of-the-art—see, e.g., Ref. [25], circularly polarized pulses with two optical oscillations, to our best knowledge, have not yet been synthesized and published. Therefore we present in Fig. 6 a CB electron distribution caused by a pulse similar to those used in GDOG [22], which contains three optical oscillations with left circular polarization followed by three oscillations with right polarization—see inset in Fig. 6. Also in this case, the CB electron population distribution is highly chiral and different for the K versus K' points, which reflects the chirality of both the optical pulse and graphene. The resulting interferograms are, understandably, more complex that for the previous cases of two optical oscillations.

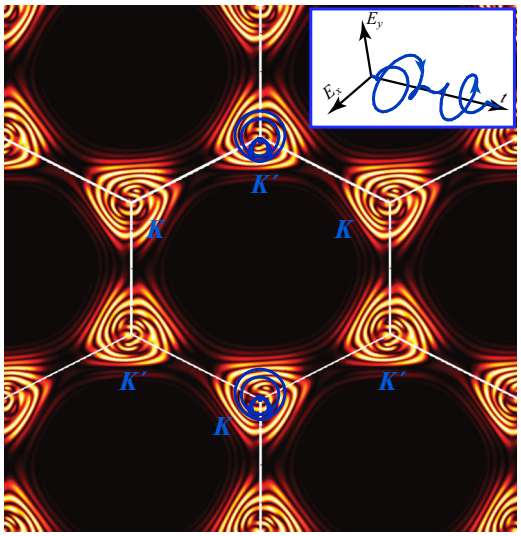

FIG. 6. Similar to Fig. 3 but for a pulse where three oscillations with left circular polarization followed by three right circularly-polarized oscillations.

IV. CONCLUSIONS

In conclusion, we have proposed a self-referenced interferometry in graphene in the reciprocal space. A strong ($\sim$0.5 V/Å) ultrashort ($\sim$5 fs) optical pulse is populating the CB on subcycle times ($\sim$100 as). Circular polarization of the pulse causes electron to circle in the reciprocal space accumulating the dynamic phase along this closed trajectory. Circling around a Dirac (K or K') point adds also the Berry phase of π or $-\pi$. The electron VB $\leftrightarrow$ CB transitions occur predominantly in the vicinity of the Dirac point. The quantum excitation *amplitudes* corresponding to different optical cycles interfere, and their fringes reflect both the dynamic and Berry phases. The fringes of *population* are due to the dynamic phase only; they are fundamentally observable using femtosecond ARPES. These fringes carry rich information of the electronic spectra and interband dynamics near the Dirac points and the chirality of the pulse. These interference fringes of electron population are identical separately for the three K points and for the three K' points and different between the K points versus the K' points. This reflects the local chirality in the reciprocal space related to the topological Berry curvature, flux, and phase.

The previous work on Berry phase interferometry in the reciprocal space [6] was done in a magnetic field gradient. In a sharp contrast, we do not employ a magnetic field (which for graphene would have been too high to be realistic). Our interfering amplitudes are those for an electron passing in the vicinity of a Dirac point at *different times*, i.e., the "slits" of our interferometer are separated *in time*, not in space (real or reciprocal). The interference fringes are separated by some crystal momentum Δk, which is, on the order of magnitude, the width of the region around a Dirac point where the interband transitions take place—this can be estimated from Fig. 2(a) as $\Delta k \sim 0.1\text{Å}^{-1}$. Correspondingly, time interval Δt between formation of the fringes can be estimated from the Bloch acceleration theorem as $\Delta t \sim \hbar\Delta k/(eF_0) \sim 150$ as—in qualitative accord with kinetics in Figs. 2(b) and 2(c). This dynamics of the interferogram formation provides an attosecond "clock" that may be useful in studying the fastest electron dynamics in nature, which takes place in graphene subjected to strong optical fields.

Fundamentally, the predicted attosecond kinetics in the reciprocal space can be visualized using ARPES with attosecond ultraviolet or XUV pulses, which are realistic at the present state of the art [26,27]. Note that in our case the goal is to measure accurately only the momentum distribution of electrons in the CB as a function of time but not the full electronic dispersion relation as in conventional continuous-wave ARPES. Therefore only the *momentum* distribution should be measured accurately; in contrast, the *energy* resolution should only be sufficient to distinguish electrons coming from the CB versus those from the VB. Because the phenomena of interest encompass a significant part of the Brillouin zone, this sufficient energy resolution is in the range from $\sim$0.1 eV, which has experimentally been achieved with optical attosecond pulses (pulse duration $\sim$300 as) [27] to $\sim$0.5 eV obtained with XUV attosecond pulses (pulse duration $\sim$100 as) [26].

Another possibility is to use ARPES to measure the resulting electron interferogram after the pulse. This will persists during a period limited by the electron collision times in the CB, which has been found to be $\sim$10 fs [16]. This would further dramatically relax requirements to temporal resolution and, consequently, improve the energy resolution needed to study the vicinity of the Dirac points. Though the sensitivity of the electron interferogram in graphene to the electron collisions, i.e., electron momentum relaxation, is potentially a limiting factor, it also has "silver lining": it can be used as a clock to monitor this ultrafast relaxation dynamics with unprecedented speed. This is defined by $\sim$100 as time of the fringe formation and $\sim$100–500 as potential temporal resolution of ultrafast ARPES (see the previous paragraph).

The proposed graphene interferometry provides an approach to extract information about both electronic and topological properties of graphene and about the strong ultrafast circularly-polarized optical pulses with potentially attosecond temporal resolution. These may provide unique opportunities for attosecond metrology and light-wave driven nanoelectronics.

ACKNOWLEDGMENTS

The work of V.A. was supported Grant No. ECCS-1308473 from NSF. This work of MIS was supported by a MURI Grant FA9550-15-1-0037 from the U.S. Air Force Office of Scientific Research and the research of HKK by Grant No. DE-FG02-11ER46789 from the Materials Sciences and Engineering Division of the Office of the Basic Energy Sciences, Office of Science, U.S. Department of Energy. Supplemental support used to acquire a state-of-the art workstation came from Grant No. DE-FG02-01ER15213 from the Chemical Sciences, Biosciences and Geosciences Division of the Office of the Basic Energy Sciences, Office of Science, U.S. Department of Energy.

[1] K. S. Novoselov, A. K. Geim, S. V. Morozov, D. Jiang, M. I. Katsnelson, I. V. Grigorieva, S. V. Dubonos, and A. A. Firsov, Nature (London) **438**, 197 (2005).
[2] Y. B. Zhang, Y. W. Tan, H. L. Stormer, and P. Kim, Nature (London) **438**, 201 (2005).
[3] A. K. Geim and K. S. Novoselov, Nat. Mater. **6**, 183 (2007).
[4] G. P. Mikitik and Y. V. Sharlai, Phys. Rev. Lett. **82**, 2147 (1999).
[5] D. Xiao, M.-C. Chang, and Q. Niu, Rev. Mod. Phys. **82**, 1959 (2010).
[6] L. Duca, T. Li, M. Reitter, I. Bloch, M. Schleier-Smith, and U. Schneider, Science **347**, 288 (2015).
[7] Y. Liu, G. Bian, T. Miller, and T. C. Chiang, Phys. Rev. Lett. **107**, 166803 (2011).
[8] A. N. Grigorenko, M. Polini, and K. S. Novoselov, Nat. Photon. **6**, 749 (2012).
[9] P. R. Wallace, Phys. Rev. **71**, 622 (1947).
[10] J. C. Slonczewski and P. R. Weiss, Phys. Rev. **109**, 272 (1958).

[11] R. Saito, G. Dresselhaus, and M. Dresselhaus, *Physical Properties of Carbon Nanotubes* (Imperial College Press, London, 1998).
[12] S. Reich, C. Thomsen, and J. Maultzsch, *Carbon Nanotubes* (Wiley-VCH, Weinheim, 2004).
[13] E. H. Hwang and S. Das Sarma, Phys. Rev. B **77**, 195412 (2008).
[14] M. Breusing, S. Kuehn, T. Winzer, E. Malic, F. Milde, N. Severin, J. P. Rabe, C. Ropers, A. Knorr, and T. Elsaesser, Phys. Rev. B **83**, 153410 (2011).
[15] E. Malic, T. Winzer, E. Bobkin, and A. Knorr, Phys. Rev. B **84**, 205406 (2011).
[16] D. Brida, A. Tomadin, C. Manzoni, Y. J. Kim, A. Lombardo, S. Milana, R. R. Nair, K. S. Novoselov, A. C. Ferrari, G. Cerullo, and M. Polini, Nat. Commun. **4**, 1987 (2013).
[17] I. Gierz, J. C. Petersen, M. Mitrano, C. Cacho, I. C. E. Turcu, E. Springate, A. Sthr, A. Khler, U. Starke, and A. Cavalleri, Nat. Mater. **12**, 1119 (2013).
[18] A. Tomadin, D. Brida, G. Cerullo, A. C. Ferrari, and M. Polini, Phys. Rev. B **88**, 035430 (2013).
[19] W. V. Houston, Phys. Rev. **57**, 184 (1940).
[20] H. K. Kelardeh, V. Apalkov, and M. I. Stockman, Phys. Rev. B **91**, 045439 (2015).
[21] Y. Aharonov and D. Bohm, Phys. Rev. **115**, 485 (1959).
[22] X. Feng, S. Gilbertson, H. Mashiko, H. Wang, S. D. Khan, M. Chini, Y. Wu, K. Zhao, and Z. Chang, Phys. Rev. Lett. **103**, 183901 (2009).
[23] F. Bloch, Z. Phys. A **52**, 555 (1929).
[24] L. D. Landau, J. Phys. **10**, 25 (1946).
[25] F. Krausz and M. I. Stockman, Nat. Phot. **8**, 205 (2014).
[26] A. Schiffrin, T. Paasch-Colberg, N. Karpowicz, V. Apalkov, D. Gerster, S. Muhlbrandt, M. Korbman, J. Reichert, M. Schultze, S. Holzner, J. V. Barth, R. Kienberger, R. Ernstorfer, V. S. Yakovlev, M. I. Stockman, and F. Krausz, Nature (London) **493**, 70 (2012).
[27] M. T. Hassan, T. T. Luu, A. Moulet, O. Raskazovskaya, P. Zhokhov, M. Garg, N. Karpowicz, A. M. Zheltikov, V. Pervak, F. Krausz, and E. Goulielmakis, Nature (London) **530**, 66 (2016).